Nanoscale

PAPER

View Article Online
View Journal | View Issue

Cite this: *Nanoscale*, 2014, **6**, 10693

The synthesis of CeO_2 nanospheres with different hollowness and size induced by copper doping†

Wei Liu, Xiufang Liu, Lijun Feng, Jinxin Guo, Anran Xie, Shuping Wang, Jingcai Zhang and Yanzhao Yang*

Received 7th May 2014
Accepted 7th July 2014

DOI: 10.1039/c4nr02485k

www.rsc.org/nanoscale

In this paper, copper-doped ceria oxides with different hollowness and size are fabricated by changing the Cu^{2+} doping concentration in the mixed water-glycol system. Results show that the copper-doped CeO_2 oxides undergo a morphology transformation from the solid nanospheres to core–shell, then to hollow nanospheres with the increase of the Cu^{2+} doping concentration. The corresponding size becomes smaller during this transfer process. The Cu^{2+} doping induced acceleration in the nucleation and growth process is further investigated. The resultant Cu^{2+}-doped CeO_2 oxides exhibit enhanced CO conversion performance and better reduction behaviors.

Introduction

Recently, designs of functional micro- and nano-materials have attracted much interest because of their wide application and potential properties in different fields such as biomedical science,[1] physics,[2] environment protection[3] and chemistry.[4] As is well known, the theories about structure–function relations act as a guide in the rational synthesis of functional micro- and nano-materials.[5] The exposure of active facets,[6] large surfaces area[7] and element composition[8] also have an influence on the performance of nanomaterials. According to this law, many methods to structurally modify micro- and nano-materials have been investigated in order to achieve innovative applications. Thus far, the facile synthesis over shape and size has emerged as a main synthetic methodology for the preparation of functional nanomaterials. In recent research, except for conventional morphological approaches,[9–13] doping-induced control of size and shape has been verified as a suitable modification to improve the function of the prepared nanomaterials. Shen *et al.* prepared Zr-doped hematite nanorods, and discovered the film thickness was influenced by the concentration of $ZrO(NO_3)_2$ in the precursor solution; moreover, Zr^{4+} doping was found to enhance the photocurrent for water splitting.[14] Lu's group discussed that the morphology of SnO_2 could be controlled by varying the concentration of the added Zn^{2+}. Moreover, the hierarchical Zn-doped SnO_2 nanocones displayed a higher response to ethanol compared with the pure urchin-like SnO_2 nanostructures based on gas sensors.[15] In fact, recently, impurity doping was found to have a crucial effect on the nucleation and growth of many functional materials, as well as the improvement of the performance, in a wide range of practical applications.

As a well-known, important, rare-earth oxide, ceria (CeO_2) has attracted particular interest in many fields such as ultraviolet blocking materials,[16] fuel cells,[17] oxygen sensors[18] and catalysis.[19] CeO_2 is especially considered to be a promising catalytic material due to its wide application in three-way catalysts (TWCs),[20] water-gas-shift (WGS) reactions[21] and light-catalyzed reaction.[22] However, it is noticed that the catalytic property of CeO_2 benefits from its good oxygen capacity (OSC), which is associated with the facile redox cycle between Ce^{3+} and Ce^{4+}. Generally, when the doped ion with similar or smaller radii was introduced to the CeO_2 lattice host by replacing Ce^{4+} ions, lattice defects increased and excess oxygen vacancies generated.[23,24] To date, many endeavors have been devoted to investigate the influence of doping elements on the corresponding better catalytic behavior of doped ceria.[8,25–29] However, literature is rare concerning the impurity doping-induced control on the morphology growth and phase transformation of the CeO_2 materials.

Even though it is encouraging that Li *et al.* once proposed controllable formation of CeO_2–ZrO_2 solid solution nanocages by a two-step method with the introduction of Zr^{4+},[30] it still remains an open challenge to establish a one-pot facile synthesis for the preparation of doped ceria with easy control

Key Laboratory for Special Functional Aggregate Materials of Education Ministry, School of Chemistry and Chemical Engineering, Shandong University, Jinan, 250100, P. R. China. E-mail: yzhyang@sdu.edu.cn; Fax: +86-531-88564464; Tel: +86-531-88362988

† Electronic supplementary information (ESI) available: Fig. S1 the TEM images of the Cu^{2+}-doped CeO_2 (a–c): P_2, P_5 and P_6; Fig. S2 EDS spectrum of the Cu^{2+}-doped ceria sample; Fig. S3 the HRTEM images about lattice fringes of the Cu^{2+}-doped CeO_2: (a and b) P_3; (c and d) P_4; Fig. S4 the corresponding XPS survey spectrum of nanospheres: P_1 and P_4; Fig. S5 XRD pattern of P_3 obtained at different solvothermal time, illustrated as (a) 1 h, (b) 2 h, (c) 4 h and (d) 8 h; Fig. S6 the TEM images of (a) the P_1 sample at 36 h and (b) the P_4 sample at 2 h; Fig. S7 N_2 adsorption–desorption isotherms of the pure and Cu^{2+} doped CeO_2: (a) P_1, (b) P_2, (c) P_3, (d) P_4, (e) P_5 and (f) P_6. Insets are the corresponding BJH pore-size distribution curves. See DOI: 10.1039/c4nr02485k

over size and shape. In our current work, a series of Cu^{2+}-doped CeO_2 spheres with different hollowness and size have been first prepared *via* a one-step, mild solvothermal process. In striking contrast to conventional techniques, which require a more cautious coordination of several experimental parameters to control the size and shape, our Cu^{2+}-doped approach only needs a single variable-Cu^{2+} doping concentration. When the Cu^{2+} concentration increased from 0 to 40 g L^{-1} in the above process, the final products changed from the initial solid spheres to core–shell spheres, then to hollow spheres obviously. The whole synthetic mechanism involved a Cu^{2+}-induced fast nucleation and a slow growth based on the Ostwald ripening in the water-glycol system. Remarkably, the as-prepared Cu^{2+}-doped CeO_2 products display better reduction behaviors and enhanced catalytic performance towards CO oxidation.

Experimental section

Materials

Cerium nitrate hexahydrate (99.9%, $Ce(NO_3)_3 \cdot 6H_2O$) was purchased from Tianjin Kermel Co. Ltd. Polyvinylpyrrolidone (PVP, K30), copper chloride dihydrate (99%, $CuCl_2 \cdot 2H_2O$), cupric nitrate trihydrate (99%, $Cu(NO_3)_2 \cdot 3H_2O$) and ethylene glycol were obtained from Sinopharm Chemical reagent Co. Ltd. All the reactants were of analytical grade and were used without further purification or modification. Deionized water and absolute alcohol were used throughout.

The synthesis of CeO_2 nanospheres (P_1)

0.5 g cerium nitrate hexahydrate ($Ce(NO_3)_3 \cdot 6H_2O$) and 0.2 g PVP were dissolved in 15 mL ethylene glycol, and then 1 mL deionized water was added to the above solution. After continuous stirring for 30 min, the clear solution was transferred into a Teflon-lined autoclave of 20 mL capacity and heated for 8 h at 160 °C. When the autoclave was cooled at room temperature, the light purple products were collected and washed with deionized water and absolute alcohol three times sequentially. Finally, the products were dried at 70 °C overnight, and then calcined at 300 °C for 1 h.

The synthesis of Cu^{2+} doped CeO_2 spheres (P_2–P_6)

0.5 g cerium nitrate hexahydrate $Ce(NO_3)_3 \cdot 6H_2O$ and 0.2 g PVP were dissolved in 15 mL ethylene glycol, and then 1 mL $CuCl_2 \cdot 2H_2O$ solution of different concentration (2, 10, 20, 30, 40 g L^{-1}) was added to the above solution. After continuous stirring for 30 min, the mixed solutions were transferred into a Teflon-lined autoclave of 20 mL capacity and heated for 8 h at 160 °C. When the autoclave was cooled to room temperature, the gray products were collected and washed with deionized water and absolute alcohol three times sequentially. Finally, the products were dried at 70 °C overnight, and then calcined at 300 °C for 1 h. The above products with different Cu^{2+} doping concentration were labeled as P_2–P_6 samples.

Characterization

The phase purity of the sample was examined by using a Bruker D8 Avance X-ray diffractometer with Cu-Kα radiation (λ = 0.15418 nm) in the 2θ range from 10° to 80°. The micro-structure and morphology of the products were characterized using a transmission electron microscope (TEM, JEM 100-CXII, 80 kV), a field-emission scanning electron microscope (FE-SEM, Hitachi, S4800) equipped with a energy-dispersive X-ray spectrometer (EDS) and a high-resolution transmission electron microscope (HRTEM, JEM-2100, 200 kV). Raman data were obtained using a LabRAM HR4800 spectrometer while using a 514 nm laser line as an excitation source. N_2 adsorption–desorption isotherms were measured on a QuadraSorb SI at 77.3 K. Before the measurement, the samples were outgassed at 200 °C under vacuum for 4 h. The surface areas were calculated by the Brunauer–Emmett–Teller (BET) method, and the pore-size distribution was calculated from the desorption branch using the Barrett–Joyner–Halenda (BJH) theory. Temperature-programmed reduction under a H_2 environment (H_2-TPR) was carried out on a PCA-1200 instrument. Typically, 50 mg CeO_2 catalyst was pretreated under 5% O_2–Ar stream at 300 °C for 0.5 h (heating rate = 5 °C min^{-1}). After cooling down to room temperature, a flow of 5% H_2–Ar was introduced into the CeO_2 sample with a flow rate of 30 mL min^{-1}, and then the temperature was increased to 500 °C at a rate of 5 °C min^{-1}.

Measurement of catalytic activity

The catalytic activity of the as-obtained samples were evaluated by a continuous flow fixed-bed microreactor operating under atmospheric pressure. In a typical experiment, catalyst particles (25 mg) were placed in the reactor. The reactant gases (1% CO, 10% O_2, and 89% N_2) passed through the reactor at a rate of 40 mL min^{-1}. The composition of the gas exiting the reactor was analyzed with an online infrared gas analyzer (Gasboard-3121, China Wuhan Cubic Co.), which simultaneously detects CO and CO_2 with a resolution of 10 ppm. The results were further confirmed with a Shimadzu gas chromatograph (GC-14).

Results and discussion

Structural analysis

Fig. 1 shows the typical diffraction patterns of the as-prepared CeO_2 products, including pure CeO_2 (P_1) and the series of Cu^{2+}-doped CeO_2 samples (P_2–P_6). The diffraction peaks of all the products illustrated that they can be well indexed to a pure phase of face-centered cubic ceria structures (JCPDS no. 34-0394). It is noticed that no other impurities, such as cerium alkoxide or copper oxide, could be found. The high purity of all products indicates the formation of homogeneous Ce–Cu–O solid solutions. Furthermore, the broadening peaks shown in Fig. 1 indicated the formation of small nanocrystallites in all products. However, Cu^{2+}-doped CeO_2 samples are composed of smaller crystallites than pure ceria because of the broader peaks.[31,32] The substitution will be ascertained in the following text.

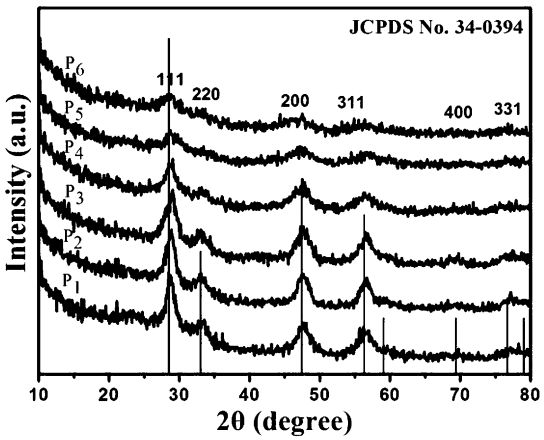

Fig. 1 The XRD patterns of the as-obtained P_1–P_6 samples.

The morphology and structures of the as-prepared P_1–P_6 samples are explored by transmission electron microscopy (TEM) and scanning electron microscopy (SEM). The low magnification TEM and SEM images of P_1 sample show that the products consist of well-dispersed uniform nanospheres with a size ranging from 180 to 240 nm (Fig. 2a and c). The magnified SEM image (Fig. 2b) makes it clear that the surface of the nanosphere is very rough, which indicates that there are many small nanoparticles on the surface. Furthermore, the high magnification technology was applied to analyze the detailed structure of the rough nanospheres (inset in Fig. 2c). The lattice fringes measured from the HRTEM image (Fig. 2d) was about 0.272 nm, which matched well with the spacing of the (200) planes of ceria. The selected area electron diffraction (SAED) pattern (inset in Fig. 2d) of a single nanosphere indicates the polycrystalline structure of the pure CeO_2.

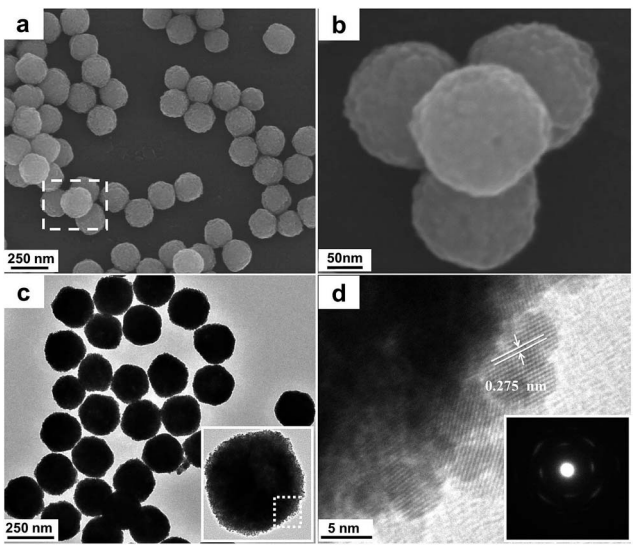

Fig. 2 The SEM and TEM images of the as-prepared undoped CeO_2 (P_1). (a) The low-magnification SEM images; (b) the high-magnification SEM image taken from the area marked in (a); (c) the TEM image; (d) the HRTEM image taken from an individual sphere, which is shown in the inset in (c); the inset image is the corresponding SAED pattern of P_1 sample.

In our experiment, an interesting phenomenon has appeared when the appropriate amount of $CuCl_2$ was introduced to the ceria host. When the concentration of $CuCl_2$ solution is lower, the core–shell spheres emerged such as P_2 and P_3 samples. However, the hollow spheres and even amorphous particles dominate in the products with an increase in the $CuCl_2$ concentration (P_4–P_6 samples). Fig. 3 and S1† provide the intuitive information of the structures and morphologies of Cu^{2+}-doped CeO_2 samples (P_2–P_6). Here, the P_3 and P_4 samples are taken as typical models to illustrate the morphology transformation. As shown in Fig. 3, several important characters can be distinguished: (1) the primary morphology (Fig. 2) disappears and is replaced by hollow structures obviously when the $CuCl_2$ was introduced. (2) The morphology and size of the as-obtained doped CeO_2 are different when the concentration of the added $CuCl_2$ solution changed. When the concentration is 10 g L^{-1}, the P_3 sample are mainly composed of core–shell spheres with an average diameter of 110 nm, which can be verified by the color contrast from the SEM and TEM images (Fig. 3A1 and A2).

Further, it is worth noting that hollow spheres (a few ones are broken) hold the biggest ratio in P_4 sample when the concentration increased to 20 g L^{-1} gradually, and its

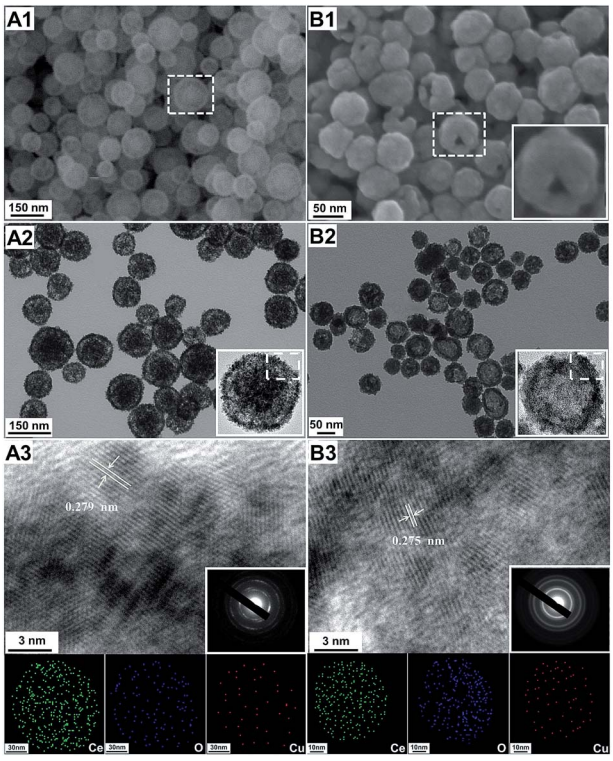

Fig. 3 The SEM and TEM images with different magnification of the as-prepared Cu^{2+}-doped CeO_2. (A1 and B1) the SEM images of P_3 and P_4; (A2 and B2) the TEM images of P_3 and P_4, the inset HRTEM image is an individual core–shell and hollow spheres respectively; (A3 and B3) the HRTEM image and SAED pattern of P_3 and P_4 taken from a single core–shell and hollow sphere, which are shown as an inset in A2 and B2; EDS-mapping image of an individual nanospheres, which is marked in Fig. 3A1 and B1: (a) Ce (green), O (blue), and Cu (red).

corresponding diameters continuously reduced to 40–80 nm (Fig. 3B1 and B2). Different types of doped ceria (P_2 and P_6) are shown in Table 1. The Cu–Ce atom ratio is highest in P_4 samples (3.8%). In addition, the EDS spectra corresponding to the doped ceria samples also are displayed in Fig. S2 (ESI).† (3) From the inset pictures of Fig. 3A2 and B2, we can see that the compact small nanoparticles are the primary building units in these two kinds of doped products. Moreover, the structures of P_3 and P_4 samples are more loose than the undoped ceria (P_1). The polycrystalline properties provided by the selected area electron diffraction (SAED) patterns from the HRTEM results of the P_3 and P_4 samples demonstrate that the products are formed of many small nanoparticles. (4) The interplanar spacing of the two planes is about 0.279 nm (Fig. 3A3) and 0.275 nm (Fig. 3B3), which are comparable to the values of the (200) plane of face-centered phase ceria. However, there are many "dark pits" and bent lattice fringes occurring in both doped products, which is shown in Fig. S3 (ESI),† and it is more obvious in the hollow spheres. According to the research of Li's group, this phenomenon indicated that the surface of the P_3 and P_4 samples is much rougher and more surface reconstruction happened in the structures transformation,[33] and this characteristic maybe useful for catalytic performance.[34] Elemental EDS-mapping images conducted on a single sphere of P_3 and P_4 samples confirmed the occurrence of homogeneous distributions of Ce, Cu and O. (5) As shown in Fig. 4, the average diameter of the products in P_1–P_6 samples decreases progressively with an increase in $CuCl_2$ concentration.

All the samples (P_1–P_6) are also characterized by the Raman spectra with the exciting laser wavelength of 514 nm, illustrated in Fig. 5. For P_1 sample (pure ceria), the observed main Raman band around 460 cm^{-1} is related to the triply degenerate F_{2g} Raman active mode of the CeO_2 fluorite structure, which is the only one allowed in first order and supported by XRD results.[35,36] For the P_2–P_6 samples, two typical characteristics in the main F_{2g} mode band, which differ from the pure ceria, can be described as follows: red shift appears and the width of peak increases because of the lattice defects[37–39] and the positions of the above band in doped samples (P_2–P_6) are different. It can obviously be seen that the peak values decrease, and then increase with an increase in the Cu^{2+} doping concentration. Note that the lowest value (432 cm^{-1}) appeared in P_4 sample when the Cu^{2+} doping concentration is 20 g L^{-1}, which is in accordance with the EDS results. The lower doping

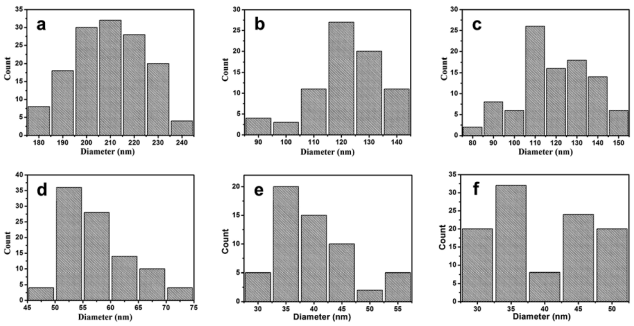

Fig. 4 The corresponding diameter distribution of the as-prepared samples: (a) P_1, (b) P_2, (c) P_3, (d) P_4, (e) P_5 and (f) P_6.

concentration in the CeO_2 host (P_5 and P_6) may be a crucial reason for the non-monotonic Raman peak shift. Additional weak peaks at around 600 cm^{-1} are also observed in the doped ceria samples (P_3 and P_4), which would be attributed to the presence of the oxygen vacancies.[40,41] The above phenomena is powerful evidence of copper incorporation in the lattice for the P_2–P_6 samples.[42] Moreover, the Cu–O characteristic peak at 294 cm^{-1} is absent in the spectrum of the P_2–P_6 samples. This agrees with the previous XRD results, which further certify the incorporation of bivalent Cu^{2+} to the CeO_2 fluorite lattice. X-ray photoelectron spectra (XPS) experiments were carried out to further determine the existence and the valence states of the elements in our samples. Fig. S4† shows the XPS spectra of the pure ceria (P_1) and the doped ceria (P_4) as the typical samples. Several typical BE peaks (such as those at 882.1, 898.5 and 916.8 eV) of the Ce 3d spectrum (Fig. S4b†) are observed in the P_1 and P_4 samples, which suggest the existence of Ce(IV) in the as-obtained products. The Cu 2p spectrum (Fig. S4d†) shows weak peaks due to the low Cu concentration, which is verified by the above EDS analysis, but it can be still determined that the valence state of Cu is +2. The XPS O 1s spectrum for the samples are also examined (Fig. S4c†). The BE peak located at a binding energy of 529.2 ± 0.4 eV is assigned to the lattice oxygen of CeO_2.[29] It is obvious that the shoulder peak at around 531 eV, corresponding to the adsorption oxygen appears in the P_1 and P_4 samples.[32] Yet this peak in the doped ceria (P_4) seems much stronger than that in the pure ceria (P_1), revealing the better capacity of oxygen storage in P_4 sample. This phenomena would be related to the catalytic oxidation activity.[32]

Table 1 N_2 adsorption–desorption characterization and the compositional data of the as prepared P_1–P_6 samples

Samples	The concentration of $CuCl_2$ (g L^{-1})	S_{BET}[a] (m^2 g^{-1})	V_{BJH}[a] (cm^3 g^{-1})	D_{BJH}[a] (nm)	Atom ratio[b] (Cu/Ce, %)
P_1	0	159.594	0.073	3.720	0
P_2	2	167.282	0.273	7.848	0.83
P_3	10	164.286	0.335	9.483	2.95
P_4	20	165.554	0.442	3.705	4.13
P_5	30	169.576	0.338	3.808	2.53
P_6	40	174.097	0.311	3.823	1.27

[a] BET and BJH data of the samples come from Fig. S8 (ESI). [b] The atom ratio (Cu/Ce) data measured by EDS Analysis.

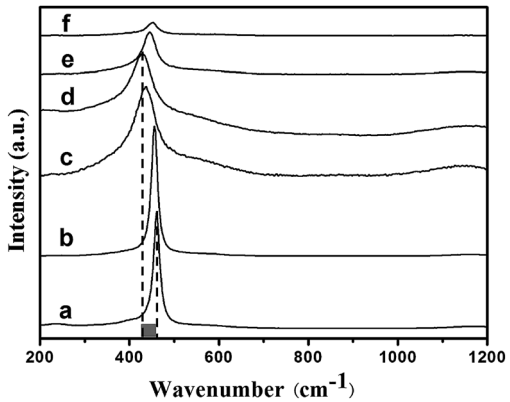

Fig. 5 Raman spectra of the synthesized P_1– P_6 (a–e).

Morphology mechanism

In order to understand the formation mechanism and the growth process better, we made a lot of effort on the morphology evolution with time-dependent experiments. For the pure ceria (P_1), the products obtained at different reaction time are studied by TEM analysis. The clear solution without precipitation was obtained after the solvothermal reaction for 1 h. As illustrated in Fig. 2, the sample P_1 contains a large amount of solid nanospheres, which are composed of small crystal grains after 10 h. However, when the reaction time is prolonged to 36 h, a homogenous hollow structure is created, even some hollow spheres are broken (ESI, Fig. S6†). For comparison, the morphology formation of the doped CeO_2 samples is also studied. Herein, when the doping $CuCl_2$ concentration is 10 g L^{-1}, the P_3 sample served as an illustrative case study. When the solvothermal reaction time was 1 h, the products were composed of loose solid spheres of uneven size ranging from 80 to 150 nm (Fig. 6a). The XRD pattern has no characteristic peaks and reveals that the sample was mainly amorphous (ESI, Fig. S5†). In the following reaction, the density decreased in the solid spheres with a coarse surface (Fig. 6b). This phenomenon is more obvious when the reaction time is 4 h (Fig. 6c). While at this time the sample could be observed with a poor crystallization. As the solvothermal process was prolonged to 8 h, the core–shell characteristic structures were shown in the Fig. 6d. Moreover, the samples could be observed with a better crystallization. The core–shell sphere still remains after 12 h. Once the reaction time increased to 16 h, the hollow spheres emerged. Furthermore, the hollow spheres appeared in the P_4 sample when the reaction time is 2 h (ESI, Fig. S6†).

According to previous literature[43-48] and the abovementioned experiments, a possible mechanism is proposed which can be concluded as the Cu^{2+}-assisted nucleation and growth based on the Ostwald ripening in the water-glycol system. As shown in Fig. 7, Ce^{3+} ions hydrolyzed initially, and they can be oxidized to Ce^{4+} by NO_3^- in the acidic environment after a short solvothermal time[49] and can be verified by the colour change from colorless clear solution to yellow. As is well known, ethylene glycol with high viscosity acts as an inhibitor, which can adsorb on the surface of small nuclei and further prevent the growth of nuclei.[29] Moreover, the concentration of water in the glycol solvent has a crucial influence on the size of ceria, which affects the nucleation and growth of ceria. The high water concentration in the glycol solvents will generate more aggregation of small particles with more regular morphology.[30] The reason lies in the increase of H_2O adsorption on the surface of small particles and the decrease of $HOCH_2CH_2OH$ adsorption. In our report, water molecules can only adsorb on the surface of Ce^{4+} when the Cu^{2+} doping concentration is 0 (P_1). However, when the concentration of Cu^{2+} doping increased (P_2–P_6), the proportion of water molecules that can adsorb on the surface of Ce^{4+} decreased, because the Cu^{2+} ion's complexation ability to H_2O shared many water molecules.[50] As a result, the relative increase in $HOCH_2CH_2OH$ adsorption on the surface of Ce^{4+} in the Cu^{2+} doped system will cause a smaller size compared with the undoped ceria (P_1). The small nuclei were attached to each other and shaped into larger aggregations in the initial stage of the high temperature sintering synthesis, with precipitates emerging earlier because of the acceleration of Cu^{2+} in the preparation of doped CeO_2 samples (P_2–P_6). In the following solvothermal process of the P_1–P_6 samples, the unstable precipitates underwent the inside-out ripening in the central part of the nanospheres. Moreover, the solid spheres became loose and the hollowness increased with the Cu^{2+} doping concentration when the reaction time is 10 h. Certainly, the detailed mechanism about the influence of Cu^{2+} needs further exploration, which will be presented in our future research.

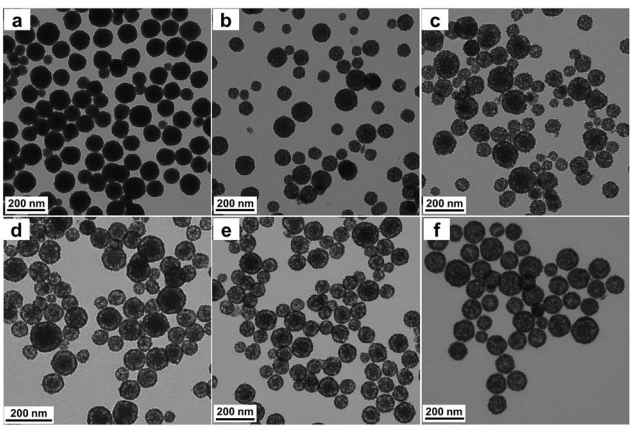

Fig. 6 The TEM images of P_3 obtained at 160 °C for different solvothermal time: (a) 1 h, (b) 2 h, (c) 4 h, (d) 8 h, (e) 12 h and (f) 16 h.

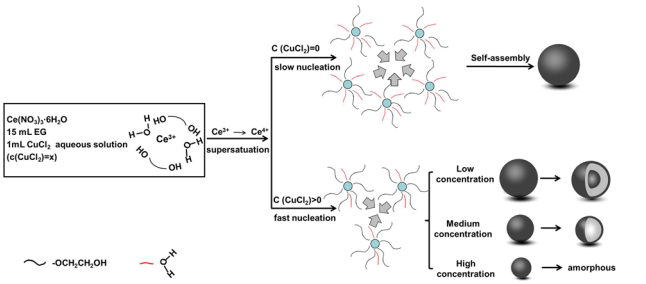

Fig. 7 Schematic illustration of the morphology evolution of Cu^{2+} doped CeO_2.

H_2-TPR reduction behaviors

The redox properties of the Cu^{2+}-doped ceria samples (P_2–P_6) were also investigated by the H_2-TPR technique (see Fig. 8). Only one broad peak with peak temperature below 350 °C can be observed in the P_2–P_6 products. The phenomena clearly presents that the reduction peak firstly shifts to a lower temperature as the Cu^{2+} doping concentration increases, and the temperature of the reduction peak is the lowest in P_4 sample. However, the temperature of the reduction peak shifts to a higher temperature when the Cu^{2+} doping concentration was further increased, which is similar to the Raman data. Previous report reveals that the pure ceria has two reduction peaks: one at 500 °C and the other above 700 °C, which can assigned to the reduction of surface oxygen and bulk oxygen respectively.[51–53] Here, the broad peak at the lower temperature can be attributed to the reduction of the Cu^{2+} ion, which is incorporated into the crystal lattice of the CeO_2 host, and the well-dispersed copper species on the surface of CeO_2.[54]

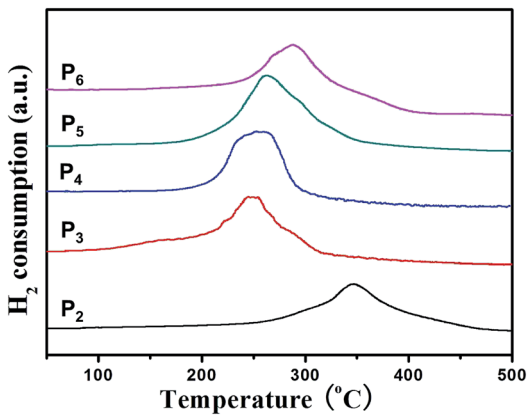

Fig. 8 The H_2-TPR profiles corresponding to the synthesized Cu^{2+} doped CeO_2: P_2–P_6 samples.

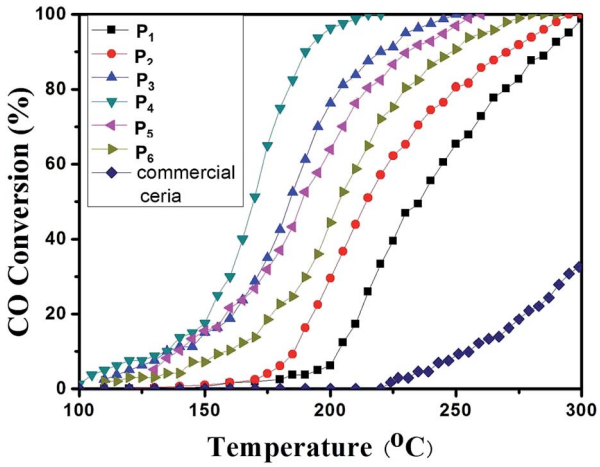

Fig. 9 Conversion of CO over commercial ceria and as-prepared P_1–P_6 samples.

Catalytic properties

CeO_2 is a good catalytic material because of its high oxygen storage capacity in the field of three-way catalysts (TWCs) over several decades.[55,56] Here, the model reaction to evaluate the catalytic property of our prepared samples is the CO conversion reaction. Fig. 9 shows the catalytic profiles of as-obtained pure ceria and doped ceria series incorporated with Cu^{2+}. Whether pure or doped ceria, it can be obviously seen that the catalytic performance of our products have been sharply improved by comparison with commercial ceria. The conversion rate of commercial ceria has failed to reach 40% at 300 °C, while all of our samples have achieved their full conversion. As shown in Table 1, the series of our samples have a large surface area, while the commercial ceria have a surface area of only 8.5 m^2 g^{-1}.[7] Thus, the surface area data can be the first evidence to explain the difference catalytic property between our products and commercial ceria as a result of the higher surface area, which can increase more active sites for conversion.[5,53] Furthermore, in our prepared products, the P_2–P_6 samples with different Cu^{2+} doping concentration show higher catalytic activity compared with the as-prepared undoped ceria (P_1). For example, the initial reaction temperature for P_4 is 100 °C and P_3 becomes active at 110 °C, whereas the P_4 sample starts to react with CO at 180 °C; furthermore, the T_{100} temperature of the prepared ceria with or without Cu^{2+} doping are as follows: 215 °C (P_4) < 250 °C (P_3) < 300 °C (P_1). With the minor difference in the surface area data, what needs to be emphasized is the large different catalytic activity among our samples. Based on the previous research, surface area is of little importance when a number of oxygen vacancies exist.[57] Here, the oxygen vacancy theory can be used to make the above question clear. The oxygen vacancies are generated in order to compensate the charge balance when the bivalent Cu^{2+} replace the tetravalent Ce^{4+} in the CeO_2 fluorite lattice.[32,58] Thus, the increased concentration of oxygen vacancies can provide the effective adsorption sites to CO gas molecules, and then guarantee the reduction property of our samples. However, the further increase of the Cu^{2+} concentration in the glycol system results in the decrease of the catalytic activity (P_5, P_6), which is supported by the Raman and H_2-TPR results. This phenomenon indicated that an appropriate doping concentration is needed in order to enhance the catalytic activity.

In order to investigate the thermal stability of Cu-doped CeO_2 products, the catalytic tests are performed in six cycles. Taking the example of the Cu-doped P_3 sample, the recycling catalytic profiles were represented and compared in Fig. 10. Obviously, the catalytic efficiency remains nearly constant during the second to sixth runs, which is even more active than that in the first run. And all the final conversion temperature is about 250 °C. Particularly, the initial starting temperature was lower by 20–25 °C, and the catalytic rates were greater than that in the first run. This can be explained by the more active sites participating in the CO conversion reaction. While the similar catalytic reaction occurred in the next run, the surface oxygen sites increased, which may promote the CO conversion.[32,59]

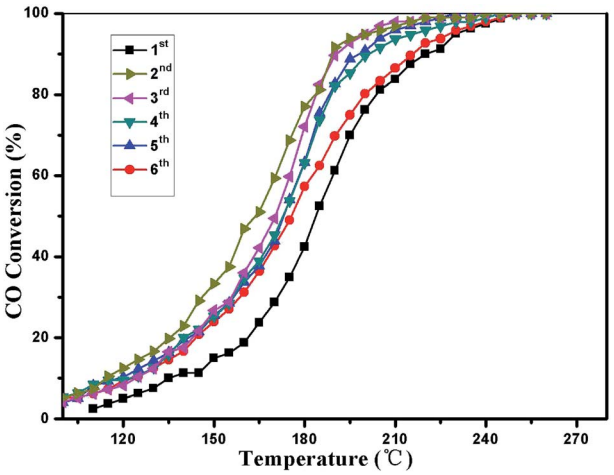

Fig. 10 Catalytic performance of the obtained P_3 in different runs.

Conclusion

In summary, we have obtained a series of designed Cu^{2+}-doped ceria nanospheres *via* a one-pot solvothermal approach. The hollowness of these samples increased with the Cu^{2+} doping concentration while the size decreased. Based on the shape evolution and formation time, the hollow nanospheres can be finally prepared. Consequently, the whole mechanism process is explored as follows: (i) in the nucleation process, the introduction of Cu^{2+} doping ions not only accelerated the nucleation rate compared with the undoped CeO_2, but also affected the adsorption proportion of $HOCH_2CH_2OH$ and H_2O molecules on the surface of the host Ce^{4+} ions. Moreover, the accelerated nucleation process by Cu^{2+} can be responsible for the smaller size of the doped ceria. (ii) The Cu^{2+} can assist Ostwald ripening occurring in the following solvothermal reaction. We hope these findings could provide a rational preparation way for novel doped CeO_2 with the desirable morphology and size, as well as other functional nanomaterials.

Acknowledgements

This work was supported by the Natural Science Foundation of China (grant nos 21276142) and the Natural Science Foundation of Shandong Province (grant nos ZR2013BM026). We would thank Prof. C. Jia for the H_2-TPR measurement.

Notes and references

1 C. D. Walkeyab and W. C. W. Chan, *Chem. Soc. Rev.*, 2012, **41**, 2780.
2 K. J. Koski and Y. Cui, *ACS Nano*, 2013, **7**, 3739.
3 S. K. Das, M. M. R. Khan, T. Parandhaman, F. Laffir, A. K. Guha, G. Sekaran and A. B. Mandal, *Nanoscale*, 2013, **5**, 5549.
4 G. R. Patzke, Y. Zhou, R. Kontic and F. Conrad, *Angew. Chem., Int. Ed.*, 2010, **49**, 2.
5 C. M. A. Parlett, K. Wilson and A. F. Lee, *Chem. Soc. Rev.*, 2013, **42**, 3876.
6 K. B. Zhou and Y. D. Li, *Angew. Chem., Int. Ed.*, 2012, **51**, 602.
7 W. Liu, L. J. Feng, C. Zhang, H. X. Yang, J. X. Guo, X. F. Liu, X. Y. Zhang and Y. Z. Yang, *J. Mater. Chem. A*, 2013, **1**, 6942.
8 C. W. Sun, H. Li and L. Q. Chen, *Energy Environ. Sci.*, 2012, **5**, 8475.
9 X. Wang, J. Zhuang, Q. Peng and Y. D. Li, *Nature*, 2005, **437**, 121; Y. C. Zhu, T. Me, Y. Wang and Y. T. Qian, *J. Mater. Chem.*, 2011, **21**, 11457.
10 H. X. Mai, Y. W. Zhang, R. Si, Z. G. Yan, L. D. Sun, L. P. You and C. H. Yan, *J. Am. Chem. Soc.*, 2006, **128**, 6426.
11 C. Wang, K. Ryu, L. G. De Arco, A. Badmaev, J. L. Zhang, X. Lin, Y. C. Che and C. W. Zhou, *Nano Res.*, 2010, **3**, 831.
12 N. Niu, P. P. yang, F. He, X. Zhang, S. L. Gai, C. X. Li and J. Lin, *J. Mater. Chem.*, 2012, **22**, 10889.
13 Y. Tian, B. J. Chen, H. Q. Yu, R. N. Hua, X. P. Li, J. S. Sun, L. H. Cheng, H. Y. Zhong, J. S. Zhang, Y. F. Zheng, T. T. Yu and L. B. Huang, *J. Colloid Interface Sci.*, 2011, **360**, 586.
14 S. H. Shen, P. H. Guo, D. A. Wheeler, J. g. Jiang, S. A. Lindley, C. X. Kronawitter, J. Z. Zhang, L. J. Guo and S. S. Mao, *Nanoscale*, 2013, **5**, 9867.
15 P. Sun, L. You, Y. F. Sun, N. K. Chen, X. B. Li, H. B. Sun, J. Ma and G. Y. Lu, *CrystEngComm*, 2012, **14**, 1701.
16 R. J. Qi, Y. J. Zhu, G. F. Cheng and Y. H. Huang, *Nanotechnology*, 2005, **16**, 2502.
17 M. Balaguer, V. B. Vert, L. Navarrete and J. M. Serra, *J. Power Sources*, 2013, **223**, 214.
18 N. Izu, T. Itoh, M. Nishibori, I. Matsubara and W. Shin, *Sens. Actuators, B*, 2012, **171**, 350.
19 G. M. Hua, L. D. Zhang, G. T. Fei and M. Fang, *J. Mater. Chem.*, 2012, **22**, 6851.
20 G. Z. Chen, F. Rosei and D. L. Ma, *Adv.Funct. Mater.*, 2012, **22**, 3914.
21 N. Yi, R. Si, H. Saltsburg and M. Flytzani-Stephanopoulos, *Energy Environ. Sci.*, 2010, **3**, 831.
22 N. Zhang, X. Fu and Y. J. Xu, *J. Mater. Chem.*, 2011, **21**, 8152.
23 R. Yousefi and B. Kamaluddin, *Appl. Surf. Sci.*, 2009, **255**, 9376.
24 S. Patil, S. Seal, Y. Guo, A. Schulte and J. Norwood, *Appl. Phys. Lett.*, 2006, **88**, 243110.
25 Y. B. Go and A. J. Jacobson, *Chem. Mater.*, 2007, **19**, 4702.
26 Y. J. Zhang, L. Zhang, J. G. Deng, H. X. Dai and H. He, *Inorg. Chem.*, 2009, **48**, 2181.
27 Z. L. liang Zhang, D. Han, S. J. Wei and Y. X. Zhang, *J. Catal.*, 2010, **276**, 16.
28 T. Y. Li, G. L. Xiang, J. Zhuang and X. Wang, *Chem. Commun.*, 2011, **47**, 6060.
29 H. Yen, Y. Seo, R. Guillet-Nicolas, S. Kaliaguine and F. Kleitz, *Chem. Commun.*, 2011, **47**, 10473.
30 X. Liang, X. Wang, Y. Zhuang, B. Xu, S. M. Kuang and Y. D. Li, *J. Am. Chem. Soc.*, 2008, **130**, 2736.
31 H. Y. Chen, A. Sayari, A. Adnot and F. Larachi, *Appl. Catal., B*, 2001, **32**, 195.
32 X. Y. Zhang, J. J. Wei, H. X. Yang, X. F. Liu, W. Liu, C. Zhang and Y. Yang, *Eur. J. Inorg. Chem.*, 2013, **25**, 4443.

33 X. W. Liu, K. B. Zhou, L. Wang, B. Y. Wang and Y. D. Li, *J. Am. Chem. Soc.*, 2009, **131**, 3140.
34 K. B. Zhou, X. Wang, X. Sun, Q. Peng and Ya. Li, *J. Catal.*, 2005, **229**, 206.
35 J. E. Spanier, R. D. Robinson, F. Zhang, S. W. Chan and I. P. Herman, *Phys. Rev. B: Condens. Matter Mater. Phys.*, 2001, **64**, 245407.
36 J. R. McBride, K. C. Hass, B. D. Poindexter and W. H. J. Weber, *J. Appl. Phys.*, 1994, **76**, 2435.
37 H. Yen, Y. Seo, S. Kaliaguine and F. Kleitz, *Angew. Chem., Int. Ed.*, 2012, **51**, 12032.
38 B. Choudhury and A. Choudhury, *Curr. Appl. Phys.*, 2013, **13**, 217.
39 W. Shan, W. Shen and C. Li, *Chem. Mater.*, 2003, **15**, 4761.
40 D. Gamarra, G. Munuera, A. B. Hungría, M. Fernández-García, J. C. Conesa, P. A. Midgley, X. Q. Wang, J. C. Hanson, J. A. Rodríguez and A. Martínez-Arias, *J. Phys. Chem. C*, 2007, **111**, 11026.
41 A. Martínez-Arias, A. B. Hungría, M. Fernández-García, J. C. Conesa and G. J. Munuera, *J. Phys. Chem. B*, 2004, **108**, 17983.
42 S. Park, J. M. Vohs and R. J. Gorte, *Nature*, 2000, **464**, 265; Z. Zhan and S. A. Barnett, *Science*, 2005, **308**, 844.
43 D. Q. Chen and Y. S. Wang, *Nanoscale*, 2013, **5**, 4621.
44 D. S. Zhang, X. J. Du, L. Y. Shi and R. H. Gao, *Dalton Trans.*, 2012, **41**, 14455.
45 Z. X. Ji, X. Wang, H. Y. Zhang, S. J. Lin, H. Meng, B. B. Sun, S. George, T. Xia, A. Nel and J. I. Zink, *ACS Nano*, 2012, **6**, 5366.
46 S. K. Meher, P. Justin and G. R. Rao, *Nanoscale*, 2011, **3**, 683.
47 M. J. Hu, J. F. Gao, Y. Dong, S. Yang and K. Y. L. Robert, *RSC Adv.*, 2012, **2**, 2055.
48 J. Cheng, X. P. Zou, W. L. Song, X. M. Meng, Y. Su, G. Q. Yang, X. M. Lu, F. X. Zhang and M. S. Cao, *CrystEngComm*, 2010, **12**, 1790.
49 X. Liang, J. J. Xiao, B. H. Chen and Y. D. Li, *Inorg. Chem.*, 2010, **49**, 8188.
50 H. J. Fan, U. G ösele and M. Zacharias, *Small*, 2007, **3**, 1660.
51 Z. L. Zhang, D. Han, S. J. Wei and Y. X. Zhang, *J. Catal.*, 2010, **276**, 16.
52 K. N. Rao, P. Bharali, G. Thrimurthulu and B. M. Reddy, *Catal. Commun.*, 2010, **11**, 8.
53 S. Y. Lai, Y. Qiu and S. Wang, *J. Catal.*, 2006, **237**, 303.
54 H. L. Mai, D. S. Zhang, L. Y. Shi, T. T. Yan and H. R. Li, *Appl. Surf. Sci.*, 2011, **257**, 7551.
55 Z. J. Yang, J. J. Wei, H. X. Yang, L. Liu and Y. Z. Yang, *Eur. J. Inorg. Chem.*, 2010, 3354.
56 S. M. Sun, X. L. Zhao, H. Lu, Z. D. Zhang, J. J. Wei and Y. Z. Yang, *CrystEngComm*, 2012, 1.
57 H. T. Chen and J. G. Chang, *J. Phys. Chem. C*, 2011, **115**, 14745.
58 Z. D. Dohcevic-Mitrovic, M. U. Grujic-Brojcin, M. J. Scepanovic, Z. V. Popovic, S. B. Boskovic, B. M. Matovic, M. V. Zinkevich and F. Aldinger, *J. Phys.: Condens. Matter*, 2006, **18**, S2061.
59 C. Zhang, L. Han, W. Liu, H. X. Yang, X. Y. Zhang, X. F. Liu and Y. Z. Yang, *CrystEngComm*, 2013, 1.

